Dynamics of Electronic States and Spin−Flip for Photodissociation of Dihalogens in Matrices: Experiment and Semiclassical Surface-Hopping and Quantum Model Simulations for F_2 and ClF in Solid Ar†

M. Bargheer,[‡] A. Cohen,[*,£] R. B. Gerber,[£,§] M. Gühr,[*,‡,#] M. V. Korolkov,[*,⊥,¶] J. Manz,[¶] M. Y. Niv,[£] M. Schröder,[¶] and N. Schwentner[‡]

Institut für Experimentalphysik, Freie Universität Berlin, Arnimallee 14, 14195 Berlin, Germany, Department of Physical Chemistry and the Fritz Haber Center for Molecular Dynamics, Hebrew University of Jerusalem, 91904 Israel, Department of Chemistry, University of California, Irvine, California 92697, Institute of Physics, National Academy of Sciences of Belarus, Skaryna Ave. 70, 220602 Minsk, Belarus, Institut für Chemie und Biochemie, Freie Universität Berlin, Takustrasse 3, 14195 Berlin, Germany, and Stanford PULSE Center, Stanford University, Stanford, California 94305

Received: March 5, 2007; In Final Form: May 21, 2007

Three approaches are combined to study the electronic states' dynamics in the photodissociation of F_2 and ClF in solid argon. These include (a) semiclassical surface-hopping simulations of the nonadiabatic processes involved. These simulations are carried out for the F_2 molecule in a slab of 255 argon atoms with periodic boundary conditions at the ends. The full manifold of 36 electronic states relevant to the process is included. (b) The second approach involves quantum mechanical reduced-dimensionality models for the initial processes induced by a pump laser pulse, which involve wavepacket propagation for the preoriented ClF in the frozen argon lattice and incorporate the important electronic states. The focus is on the study of quantum coherence effects. (c) The final approach is femtosecond laser pump−probe experiments for ClF in Ar. The combined results for the different systems shed light on general properties of the nonadiabatic processes involved, including the singlet to triplet and intertriplet transition dynamics. The main findings are (1) that the system remains in the initially excited-state only for a very brief, subpicosecond, time period. Thereafter, most of the population is transferred by nonadiabatic transitions to other states, with different time constants depending on the systems. (2) Another finding is that the dynamics is selective with regard to the electronic quantum numbers, including the Λ and Ω quantum numbers, and the spin of the states. (3) The semiclassical simulations show that prior to the first "collision" of the photodissociated F atom with an Ar atom, the argon atoms can be held frozen, without affecting the process. This justifies the rigid-lattice reduced-dimensionality quantum model for a brief initial time interval. (4) Finally, degeneracies between triplets and singlets are fairly localized, but intertriplet degeneracies and near degeneracies can span an extensive range. The importance of quantum effects in photochemistry of matrix-isolated molecules is discussed in light of the results.

I. Introduction

The concept of the cage effect has played a pivotal role in the study of photochemical reactions in condensed phases since the early years of the field. Topics such as the exit of reaction products from the cage or energy loss of the photoexcited molecule to the cage walls have been extensively studied both experimentally and theoretically, and they continue to be of major current interest. A great deal of insight has been gained on these aspects of the topic that can be described as the "mechanical" cage effects. The dynamics of the electronic states in such processes, which can be referred to as "the electronic cage effects", is much less understood. The questions of interest are many and include the following: What are the populations of different electronic states of the photoexcited species, and how do they change in time? Is there any selectivity in the electronic transitions with respect to the electronic quantum numbers? Are there any common propensities of the electronic cage effects for different systems?

A convenient framework for exploring these questions is the photochemistry of small molecules trapped in noble gas matrices (or in finite noble gas clusters). Such systems have long served as a useful laboratory for experimental and theoretical investigations of many aspects of the cage effect.[1,2] Theoretical studies of the electronic state dynamics in molecular photodissociation in matrices are, however, relatively recent. Modeling by classical molecular dynamics simulations was pursued in the early stages of the subject by treatments using only a single, excited-state potential energy surface and have remained useful for many purposes.[3−10] Such models allow, of course, only the exploration of "mechanical" aspects of the cage effect, depending on the selected electronic state. Simulations of this type cannot describe, for instance, recombination of photodissociation fragments onto the ground electronic state, a fundamental process in condensed-phase photochemistry. Molecular dynamics simulations of molecular photodissociation in matrices that include multiple potential energy surfaces and nonadiabatic

† Part of the "Sheng Hsien Lin Festschrift".
‡ Institut für Experimentalphysik, Freie Universität Berlin.
£ Hebrew University of Jerusalem.
§ University of California.
⊥ National Academy of Sciences of Belarus.
¶ Institut für Chemie und Biochemie, Freie Universität Berlin.
# Stanford University.

10.1021/jp071771t CCC: $37.00
Published on Web 07/13/2007

transitions between the different electronic states were more recently carried out by Gersonde and Gabriel,[11] Batista and Coker,[12,13] Krylov and Gerber,[14] and by Alberti et al.[15] Several closely related systems involving nonadiabatic processes were also studied by such simulations.[16,17] For our purpose here, it is important to note that, at least in several of the systems studied, nonadiabatic transitions were found to play a major role on ultrafast time scales, with significant implications also for mechanical aspects of the cage effect. In the case of HCl in solid argon, for instance, nonadiabatic transitions strongly affect the cage exit probabilities,[14] and for HCl in argon clusters, both the cage exit probabilities and the kinetic energy distribution of the H atoms exiting from the clusters are strongly influenced by nonadiabatic transitions.[18−21]

Experimentally, the study of molecular photodissociation in matrices has benefited enormously from the introduction of femtosecond pulsed laser techniques.[22−29] Such experiments proved capable of throwing light on the dynamics of electronic transitions in these processes and, in some cases, in the interaction with theoretical simulations.[30−33] An example closely related to the topics of the present paper are the combined experimental and theoretical studies by Niv et al.[31] and by Bargheer et al.[32,33] on F_2 and ClF in solid Ar, in which the effect of "ultrafast spin-flip" was found. Thus, in pump−probe pulsed laser experiments on ClF in solid argon (ClF@Ar) and in the corresponding theoretical calculations, very fast buildup of population in a $^3\Pi$ state was observed, following the initial excitation into the $C^1\Pi_1$ state.[31−33] The ultrafast spin-flip, on a time scale of less than 100 fs, is surprising at first view in this case since the spin−orbit coupling is modest. Furthermore, using a quantum model of reduced dimensionality, Korolkov and Manz showed that the rapid spin-flip can support cage exit,[34] and it may be controlled by exploiting interference effects of laser-driven coherent wavepacket dynamics.[35]

The objective of the present paper is to unravel, much more systematically, the mechanisms and rates of the nonadiabatic transitions in these systems and their effects on the populations of the different electronic states. In particular, we explore the role of the approximate quantum sublevels Ω in this process, which turn out to be of considerable importance. The prediction of ultrafast transitions between triplets with different quantum numbers motivates experimental studies of such transitions. The study also examines the role of triplets other than $^3\Pi$ in this process, namely, the $^3\Sigma$ and $^3\Delta$ triplets states, and the participation of the singlet states which are accessible to the system. The approach is based on extensive combination of pulsed laser experiments, semiclassical molecular dynamics surface-hopping simulations, and reduced-dimensionality quantum mechanical wavepacket models for the nuclear motions on coupled potential energy surfaces. These approaches overlap, in part, on some aspects of the problem but also support each other in providing complementary information.

The structure of the article is as follows. In section II, the theoretical and experimental methods used are discussed. Section III presents the main results obtained, with interpretation of the mechanisms and processes, followed by concluding remarks in section IV.

II. Systems and Methods

II.A. Semiclassical Surface-Hopping Molecular Dynamics Simulations. The simulations were carried out for F_2 in solid argon, for which system potential energy surfaces are available from previous studies.[31,36] The accumulated experience with these potential surfaces and the evidence as to their validity make this system an advantageous choice from a theoretical point of view. It seems reasonable to assume that this system can serve, at least, as a semiquantitative model for ClF in argon, which has emerged as the experimental system of choice.

The potential energy surfaces developed in ref 31 for F_2@Ar and used also here are based on the DIM (diatomic-in-molecules) method.[37] The interactions between the F atoms in the Hamiltonian use a simple electronic structure model, with a single unpaired explicit electron in a p-type orbital on each of the fluorine atoms. A valence-bond scheme was employed to describe the interactions due to the two explicit electrons in the space of p orbitals and for all possible arrangements of the spins. This led to a manifold of 36 states, including the ground state. The $^3\Pi$ states of F_2 are weakly bound, while all other excited states in this manifold are repulsive.[31,36] The interactions between the F_2, whether in the ground or an excited state, with the argon atoms were modeled by empirical potentials, taken as the sum of electronic interactions between each argon and fluorine atom, the latter described in the F(^{2}P) state. Thus, the Ar/F(^{2}P) interactions that contribute to the electronic Hamiltonian are anisotropic, reflecting the nature of the p-type orbital occupied by the unpaired electron of the F atom. The dependence of the Ar/F(^{2}P) interactions on the orientation angle between the p orbital and the Ar/F distance vector, as well as on the Ar−F distance, was taken from the gas-phase scattering experiments.[38,39] This was also checked against high-level ab initio calculations for Ar/F(^{2}P). The interactions adopted for use in the Hamiltonian were weighed in both the experimentally determined potentials and the ab initio results.[31,36] The extensive experimental and theoretical input available for Ar/F(^{2}P) gives confidence in the reliability of the potentials developed. Another contribution to the DIM Hamiltonian used for F_2@Ar is the spin−orbit coupling. This interaction is described in the DIM model used as due to the individual F atoms only and independent of the distance between them. Finally, the Ar−Ar interactions were modeled by pairwise additive potentials.[31]

In this work, as in refs 31 and 36, the 36 potential energy surfaces were obtained by diagonalizing the DIM 36 × 36 Hamiltonian matrix at each relevant configuration of the nuclei. This also yielded the adiabatic electronic states, which are denoted by $\psi_i(r,R)$, where r denotes the electronic degrees of freedom and R is the nuclear configuration. The calculation of the potential energy surfaces and adiabatic wave functions was done "on the fly" along the propagation of the trajectory of the nuclei, $R(t)$. The electronic wave function of the system at time t is represented as

$$\Psi(r,t) = \sum_i C_i(t)\psi_i(r,R(t)) \tag{1}$$

The electronic wave function evolves under the DIM Hamiltonian $H_{el}(r,R(t))$. The time-dependent Schrödinger equation, which leads to equations for the evolution of the coefficients $C_i(t)$,[31,36] describe transitions between the adiabatic electronic states $\psi_i(r,R)$, with probabilities of $P_i(t) = |C_i(t)|^2$. The coupling coefficients in the equations that describe the nonadiabatic transitions are given by[31]

$$D_{ki} = \frac{\langle \psi_k(r,R)|\nabla_R H_e(r,R)|\psi_i(r,R)\rangle_r}{V_i(R) - V_k(R)} \tag{2}$$

where $V_i(R)$ are $V_k(R)$ are the i and k adiabatic potential surfaces, respectively. The kinetic coupling vector matrix elements D_{ki}, which are functions of R, have the dimensionality of the number of nuclear degrees of freedom.

The nuclear motion dynamics, combined with the nonadiabatic transitions between electronic states, is pursued in the calculations here by a variant of Tully's "surface-hopping" algorithm.[40,41] Suppose that at $t = 0$, the system is in the k electronic state; thus, $C_k(t = 0) = 1$ and $C_{i\neq k}(t = 0) = 0$. The nuclei are propagated on the potential energy surface $V_k(R)$ using a standard classical trajectory algorithm. Using this $R(t)$, the equations for the coefficients $C_k(t)$ are solved.[36] As $|C_k(t)|$ decreases and another coefficient, or coefficients, increases, a decision according to a stochastic criterion is made on a possible transition to some other electronic (adiabatic) state j. The nuclei are then propagated on the potential surface $V_j(R)$, and the equations for the coefficients $C_j(t)$ are also solved, until the next surface-hopping event is decided upon. The specific criterion used in the surface-hopping algorithm and implemented here is Tully's "fewest switches" prescription.[40] The detailed implementation and the choice of conditions for the reinitiation of the trajectories and coefficients after a surface-hopping event are discussed in ref 31. Several other methods and algorithms have been proposed for the semiclassical treatment of nonadiabatic transitions.[41−47] While some have a more rigorous basis than that of the surface-hopping approach, the more accurate methods are computationally much harder to apply for simulations of complex many-particle systems, as in the case here. Furthermore, the experiences with surface-hopping simulations for systems of this type[14,18−21,31,32,36] have been quite encouraging.

The model system pursued in the simulations is a F_2 molecule embedded in a solid slab of 255 argon atoms, with periodic boundary conditions at the ends. Previous studies of nonadiabatic molecular dynamics simulations were carried out for F_2 in the Ar_{54} cluster.[31−33] The latter system has two layers of argon around the impurity. We obviously expect the present larger model, with the important addition of periodic boundary conditions, to more realistically describe the matrix system. Nevertheless, we shall show that the periodic boundary conditions imply certain restrictions on the time interval of the validity of the results, for example, the mechanical cage effect may involve the induction of a shock wave, which penetrates to domains beyond the slab of 255 atoms, but this may appear as an artificial shock wave that returns to the origin, mediated by the periodic boundary conditions. In practice, it turns out that the results of the present semiclassical simulations are valid during ~400 fs. Comparison with previous results for $F_2@Ar_{54}$ is instructive and will be briefly discussed later.

In the simulations, the system was first propagated in the electronic ground state until equilibrium set in (approximately 5 ps). The main set of simulations were carried out for $T = 8$ K. After equilibration, snapshots of the trajectories were taken at fixed time intervals and examined for the possible occurrence of photoexcitation to the $^1\Pi_{1u}$ state. For this, vertical promotion of the nuclei was considered, in the spirit of the classical Franck−Condon (FC) principle, at the configuration of the snapshot. The excitation energy considered in the main set of simulations was 4.6 eV. A set of 49 accepted excitation events were propagated, starting from the initially excited $^1\Pi_{1u}$ state, allowing for all possible nonadiabatic transitions, cage exit, recombination events, and so forth. In addition to the above, simulations were carried out for other types of physical conditions to address questions on several properties of the system and states involved.

Finally, we briefly discuss an instrument of interpretation employed here. The adiabatic electronic states are very convenient in the computational methodology and were employed in all simulations. However, these states are not necessarily very convenient for qualitative interpretation purposes and may have little intuitive appeal. For example, these states, which are eigenstates of the DIM Hamiltonian, are not strictly singlet or triplet states, but rather mixed. Also, these states do not always correspond simply to the states of the bare, free molecule since the DIM Hamiltonian includes interactions with the matrix atoms. We therefore found it useful to compute also the projections of the adiabatic states on the states of the free molecule (M)

$$S_{li}^{(M)}(R) = \langle \phi_l^{(M)}(r,R) | \psi_i(r,R) \rangle_r \qquad (3)$$

where $\phi_l^{(M)}(r,R)$ is the l electronic state of the free F_2 molecule. The only R coordinate on which $\phi_l^{(M)}$ depends is, of course, the internuclear distance, while ψ_i depends parametrically on the coordinates of all of the nuclei of the system. $P_{li}^{(M)}(R) = |S_{li}^{(M)}(R)|^2$ obviously represents the probability of the F_2 in the matrix to be found in the lth electronic state of the free molecule when the matrix system is in the ith adiabatic state. A given adiabatic state may, at any point in time, have significant projections onto several bare-molecule states. Such projections can differ in magnitude also for cases where nonadiabatic transitions do not take place.

It should be also noted that in the surface-hopping approach, we do not invoke directly the spin−orbit between pure spin states. Rather, both the spin−orbit coupling and the electrostatic interactions are included in the adiabatic potential surfaces and in the derivative nonadiabatic couplings, which are only indirectly connected to matrix elements of the spin−orbit interactions.

II.B. Reduced-Dimensionality Quantum Model. In addition to the preceding semiclassical surface-hopping approach, we shall also present results for complementary quantum simulations of the laser-driven photochemistry for the model system, ClF in Ar. Unlike the full dimensionality in which the semiclassical simulations are carried out, quantum simulations require simpler reduced-dimensionality models.[48] Fortunately, the semiclassical results presented in the next section for F_2 in Ar solid suggest that, indeed, a reduced one-dimensional (1D) quantum model can be employed for a short initial time interval. This model of six states, that is, the ground $X^1\Sigma_0^+$ and five excited electronic states, can describe the quantum dynamics induced by a laser pulse with a duration of $t_p = 50$ fs, which has been designed for excitation of the $C^1\Pi_1$ state, starting at $t = 0$ until about 85 fs, that is, during ~60 fs after the laser peak intensity. It turns out that the argon matrix is essentially frozen during this initial period, in which the dihalogen bond is stretched following photoexcitation until the halogens hit the Ar cage atoms and transfer kinetic energy to them.[33,34] The dynamics of the entire system is thus reduced to the dynamics of the dihalogen bond coordinate R while keeping all other degrees of freedom frozen in the initial equilibrium configuration. For reference, we shall consider the case of the preoriented dihalogen molecule along the <111> direction of the Ar matrix, as essentially for F_2 in Ar, compared with ref 49. In the case of F_2 in Ar, this initial period lasts for approximately 40 fs after excitation of the $C^1\Pi_1$ state; see section III. This result of the semiclassical surface-hopping method is in good agreement with quantum simulations of the laser-driven dynamics of F_2 interacting with the neighboring Ar atoms, specifically with those which form the "windows" for exit of the F atoms out of the Ar matrix cage.[50] Complementary quantum simulations for the laser-driven stretch of ClF excited to the $C^1\Pi_1$ state in Ar show that its

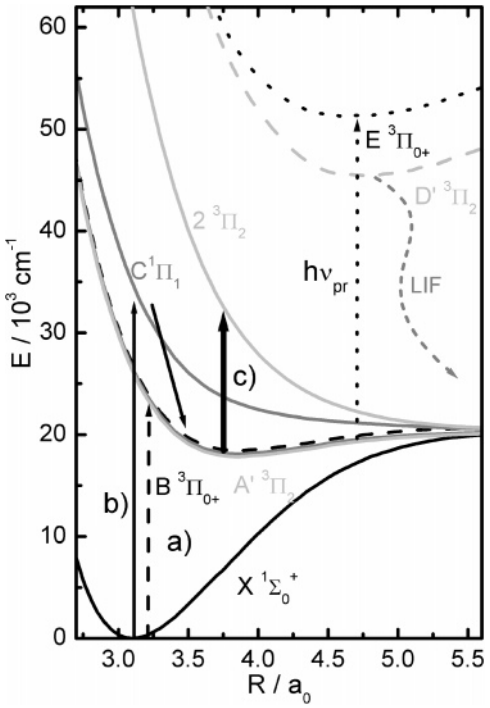

Figure 1. Potential energy surfaces of ClF in the gas phase and solvated D′ state, adapted from refs 32 and 52. Transitions a, b, and c are described in the text and in Figure 3.

center of mass starts to move in the matrix cage approximately 60 fs after the peak intensity of the exciting laser pulse due to the interactions of the F and Cl atoms with the matrix cage.[34] Accordingly, the validity of the 1D model during the initial period is slightly longer for ClF than that for F_2. This is also supported by the experimental results, which show that after photoexcitation of ClF in Ar, it takes more than 150 fs before the stretch of the ClF bond is reversed by the matrix environment.[33] Several reasons explain the longer experimental period (∼150 fs) compared to the theoretical one (∼85 fs). First, the experimental scenario corresponds to different orientations (preferably along <100>[49]), in contrast with the assumed <111> orientation of the 1D quantum model, implying somewhat larger experimental domains for the ClF stretch compared to that of the 1D quantum model. Second, energy transfer from the ClF bond stretch to the motion of the center of mass of ClF in the matrix cage causes a slow-down of the bond stretch.[50] Third, energy transfer to the environment, in particular, to Ar atoms causing "head-on-collisions" but also to others, causes further delays of the experimentally observed period of the initial bond stretch compared to that of the 1D quantum model.[51,52] Irrespective of the different time scales, however, all systems exhibit similar mechanisms of electronic cage effects, to be discovered below. In the subsequent applications, nevertheless, we shall show results for the 1D model up to 150 fs in order to discuss some systematic trends while keeping in mind that the 1D model is only valid until about 85 fs. One trend of the duration of the validity of the 1D model with increasing masses is also confirmed by investigations of the heavier dihalogens embedded in Ar; for Cl_2, it is about 150 fs.[51] The validity of the 1D model depends, of course, not only on the atomic masses but also on the potential surface details of the relevant excited states. For example, if ClF is excited initially to the $B^3\Pi_{0^+}$ state, then the validity duration of the 1D model is longer than 85 fs for excitation of the initial $C^1\Pi_1$ state because, in the Franck−Condon domain, the repulsive forces are weaker and the ClF bond stretch is slower for $B^3\Pi_{0^+}$ than for $C^1\Pi_1$.

The laser-driven quantum simulations include six nuclear wavepackets. These wave functions, $\Psi_i(R,t)$, $i = 1-6$, correspond to six electronic states, the ground state, $X^1\Sigma_0^+$, a set of four excited triplet states, $A'^3\Pi_2$, $A^3\Pi_1$,$1^3\Pi_{0^-}$, and $B^3\Pi_{0^+}$, and the excited singlet state $C^1\Pi_1$. The four triplets are lying energetically between the two singlet states. The wavepackets $\Psi_i(R,t)$ are evaluated as solutions of the time-dependent Schrödinger equation

$$i\hbar\frac{\partial}{\partial t}\begin{pmatrix}\Psi_1(R,t)\\ \Psi_2(R,t)\\ \Psi_3(R,t)\\ \Psi_4(R,t)\\ \Psi_5(R,t)\\ \Psi_6(R,t)\end{pmatrix} = \begin{pmatrix} T+\tilde{V}_1 & 0 & 0 & 0 & 0 & -\mu_{16}\cdot E(t)\\ 0 & T+\tilde{V}_2 & \gamma_{23} & \gamma_{24} & \gamma_{25} & g_2\\ 0 & \gamma_{32} & T+\tilde{V}_3 & \gamma_{34} & \gamma_{35} & g_3\\ 0 & \gamma_{42} & \gamma_{43} & T+\tilde{V}_4 & \gamma_{45} & g_4\\ 0 & \gamma_{52} & \gamma_{53} & \gamma_{54} & T+\tilde{V}_5 & g_5\\ -\mu_{61}\cdot E(t) & g_2 & g_3 & g_4 & g_5 & T+\tilde{V}_6 \end{pmatrix}\cdot \begin{pmatrix}\Psi_1(R,t)\\ \Psi_2(R,t)\\ \Psi_3(R,t)\\ \Psi_4(R,t)\\ \Psi_5(R,t)\\ \Psi_6(R,t)\end{pmatrix} \quad (4)$$

where $T = (-\hbar^2/2m)\cdot(\partial^2/\partial R^2)$ accounts for the kinetic energy of the dihalogen bond stretch R with reduced mass $m = (m_F m_{Cl})/(m_F + m_{Cl})$. The $\tilde{V}_i(R)$ (i =1, ..., 6) values denote diabatic potential energy surfaces depending on R and are evaluated for the fixed initial equilibrium geometry of the argon matrix. Furthermore, we assume that the excited singlet state ($j = 6$) is coupled to the triplet states, $i = 2$, ..., 5 by means of potential couplings $g_i = \tilde{V}_{i6}$ ($i = 2$, ..., 5), and the triplet states are coupled among each other by means of potential couplings $\gamma_{ij} = \tilde{V}_{ij}$, $2 \le i, j \le 5$.

The generation of the present diabatic from the adiabatic potentials requires, in principle, two steps. First, one calculates pure adiabatic singlet or triplet states of the dihalogen in the rare-gas matrix, taking into account spin−orbit coupling between these states as off-diagonal matrix elements. As a consequence, the laser excitation is described in terms of laser dipole coupling exclusively between the pure singlet ground state ($j = 1$) and the excited state ($i = 6$). This allows illuminating interpretations of quantum simulations of the laser-driven dynamics; for example, excitations of the spin-forbidden transition to the excited triplet state $B^3\Pi_{0^+}$ appears as an ultrafast sequential process, that is, off-resonant excitation of the singlet state $C^1\Pi_1$ followed by almost instantaneous transition to the triplet state $B^3\Pi_{0^+}$, which is mediated by spin−orbit coupling. Note that in the semiclassical simulations, these laser excitations are approximated as instantaneous Franck−Condon (FC)-type transitions.

The corresponding adiabatic potential energy curves of the pure spin states $X^1\Sigma_0^+$, $B^3\Pi_{0^+}$, and $C^1\Pi_1$ are adapted from refs 32 and 52 based on the DIM approach, with underlying ab initio results for the pure adiabatic singlet and triplet states of ClF in

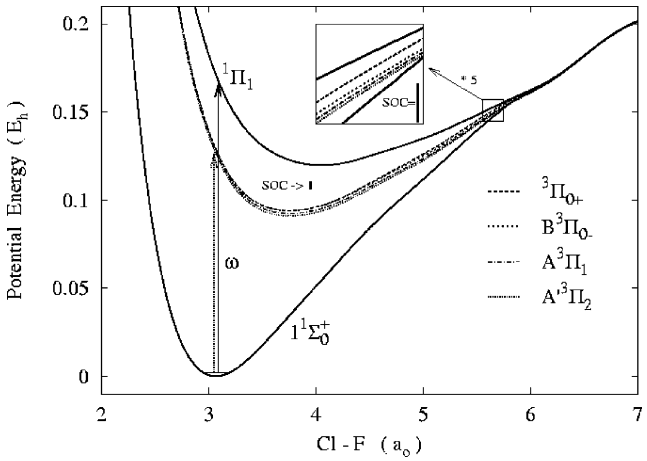

Figure 2. Diabatic potential energy curves for the lowest six singlet and triplet states of the 1D ClF@Ar model oriented along the <111> direction, adapted from refs 32, 52, and 53.

the gas phase.[53] The latter are shown, for reference, in Figure 1 together with schematic potential curves for the excited ionic states of ClF in Ar. The energy gaps between the ab initio potential curves for the $B^3\Pi_{0^+}$ state and the other three neighboring triplet states are very small, and therefore, they are in an energetic resonance. Thus, we have employed the same energy gaps also for the corresponding four triplet states of ClF in the Ar matrix.

In the second step, the kinetic couplings between these pure adiabatic triplet or singlet states are transformed into corresponding potential couplings of either the pure singlet or triplet diabatic potentials, without any additional potential couplings between pure singlet and triplet potentials. The effect of this adiabatic-to-diabatic transformation is larger for the off-diagonal matrix elements than that for the diagonal ones. Hence, for simplicity, we set the diagonal diabatic potential equal to the adiabatic ones, adopted from refs 33 and 50. The potential curves, $\tilde{V}_i(R)$, $i = 1-6$, are shown in Figure 2. Note that, in the previous semiclassical approach, the effect of the kinetic couplings between adiabatic states is taken into account approximately in terms of the surface-hopping algorithm for the classical trajectories.

The diabatic potentials $\tilde{V}_i(R)$ are then complemented by the off-diagonal diabatic potential couplings $\tilde{V}_{ij}(R)$, as follows. (a) The excited singlet state ($j = 6$) is coupled to the triplet states only by spin−orbit couplings, denoted as $\tilde{V}_{i6} = g_i$ for $i = 2, ..., 5$. In principle, there are also analogous spin−orbit couplings between the electronic ground state ($j = 1$) and the excited triplet states, but these are neglected in the present simulations. (b) The diabatic potential couplings between the manifold of the triplet states is denoted as $\tilde{V}_{ij} = \gamma_{ij}$ for the pure diabatic triplet states, $2 \le i, j \le 5$. These γ_{ij} should be considered as effective diabatic couplings, which account not only for the kinetic couplings but also for other effects, which are not included in an ideal 1D model of ClF oriented along <111> in Ar, for example, effects of other orientations. In any case, we expect the absolute values of the γ_{ij} to be smaller than those for g_i. There are analogous diabatic potential couplings γ_{16} between the singlet ground ($i = 1$) and excited ($j = 6$) states, but again, these are neglected for the present quantum simulations. In practice, however, we do not calculate these couplings g_i and γ_{ij} explicitly. Instead, we shall explore the effects of these couplings for various scenarios, from vanishing via small to large diabatic couplings. (c) Last but not least, the laser coupling of the electronic ground ($i = 1$) and excited singlet ($j = 6$) states is described by means of the semiclassical transition dipole coupling $-\mu_{16}(R)\cdot E(t)$, where $\mu_{16}(R)$ and $E(t)$ are the components of two parallel vectors representing the transition dipole and the electric field, assuming polarization perpendicular to the molecular bond. Here, we use the ab initio results for $\mu_{16}(R)$.[53]

The electric field of the laser pulse is described by

$$E(t) = E_0 \cdot s(t) \cdot \cos(\omega t) \tag{5}$$

with an amplitude E_0, carrier frequency ω, and shape function

$$s(t) = \sin^2(\pi \cdot t/t_p) \quad 0 \le t \le t_p \tag{6}$$

where t_p denotes the pulse duration. The corresponding intensity of the laser pulse (averaged over the carrier cycles) is

$$\tilde{I}(t) = \frac{1}{2}\epsilon_0 c E_0^2 s^2(t) \tag{7}$$

and has a maximum value of $\tilde{I}_{max} = (1/2)\epsilon_0 c E_0^2$ and temporal and spectral width of $\Delta t_p = 0.364 \cdot t_p$ (fwhm) and $\Gamma \approx 3.3 \cdot \hbar/\Delta t_p$, respectively.

The wavepackets $\Psi_i(R,t)$ are propagated on spatial and temporal grids $R_j = R_0 + j\cdot\Delta R$, $j = 0, ..., N_g$ (typically, $N_g = 1024$, $R_0 = 2a_0$, $\Delta R \le 0.1a_0$) and $t_l = l\cdot\Delta t$, ($\Delta t \approx \hbar/E_h \approx 0.024$ fs). For this purpose, the coupled eq 4 is solved numerically using the $O(\Delta t^3)$ split-operator technique[54] and the fast Fourier transform (FFT) method[55] for transformation between coordinate and momentum space. The resulting populations of the electronic states are calculated as $P_i(t) = \int|\Psi_i(R,t)|^2 dR$, and they are normalized according to

$$\sum_{i=1}^{6} P_i = 1$$

Initially, the system is prepared in the vibrational ground state $\Psi_i(R,t=0) = \delta_{i1}\cdot\Phi_{i=1,v=0}(R)$ of the electronic ground state. It is computed by means of the Fourier grid Hamiltonian method.[56]

II.C. Experiments. Ultrafast spin-flip has been demonstrated experimentally for ClF, showing a nonradiative transition from the repulsive $C^1\Pi_1$ state to the bound $^3\Pi$ manifold in refs 32 and 33. The intention here is to additionally investigate another member of the manifold of repulsive triplet states in order to reveal systematic trends as well as peculiarities of specific states. In particular, motivated by the theoretical results, we shall investigate transitions between triplet states. Nonradiative transitions are induced in these ultrafast pump−probe experiments by selectively exciting the initial state with a short pump pulse, thus generating a propagating wavepacket. The feeding dynamics from the excited state into the target state is monitored by a time-delayed probe pulse, which carries the wavepacket in the target state at a well-defined internuclear distance to the charge-transfer states of ClF and by finally recording the laser-induced fluorescence (LIF) intensity from these charge-transfer states versus the time delay (curved arrow in Figure 1).

It is necessary to tune the central wavelengths of the pump and probe pulses according to the requirements of the electronic transitions. To ease the comparison of the new results with the previous ones, we use the same preparation of the ClF-doped Ar films[57] and the same laser setup with two tunable NOPA devices used in refs 32 and 33 and described in ref 27. The spectroscopic characterization of the relevant states of ClF in an Ar matrix has also been carried out in ref 57, and we use these results in order to select the appropriate pump and probe pulses. The potential energy surfaces of ClF in the gas phase

are depicted in Figure 1; the charge-transfer states are red shifted with respect to the gas phase due to the influence of the matrix.

The target states are the bound triplet states, which are in energetic order $A'^3\Pi_2$, $A^3\Pi_1$, $1^3\Pi_{0^-}$ and $B^3\Pi_{0^+}$. The internuclear distance $R \approx R_p$ of the probe window position is determined by the difference potential $\Delta V(R)$ between the charge-transfer state and the target state and the probe photon energy $h\nu_{pr}$ via $\Delta V(R_p) = h\nu_{pr}$. For the $B^3\Pi_{0^+}$ target state, a strong probe transition to the $E^3\Pi_{0^+}$ charge-transfer state is observed, as expected from the dipole selection rules. A frequency-doubled probe pulse from the NOPA with a wavelength of 318 nm was used in the previous experiments,[32,33] and for consistency, it is employed also here. It corresponds to a probe window position R_p around $4.7a_0$ according to Figure 1, assuming that the repulsive contributions from the cage wall (which are not included in Figure 1) are similar for the states involved.

All $^3\Pi \leftrightarrow X^1\Sigma_0^+$ transitions violate the spin selection rule. Moreover, the $A'^3\Pi_2 \leftrightarrow X^1\Sigma_0^+$ violates the Ω selection rule, having $\Delta\Omega = 2$. Therefore for all interhalogens, a trend of increasing radiative lifetimes corresponding to a decrease in transition moments from the microsecond range for the $B^3\Pi_{0^+}$ state to milliseconds for the $A'^3\Pi_2$ state is well-known. Population of the $B^3\Pi_{0^+}$ state of ClF leads to a radiative decay with a lifetime of 141 ms exclusively from the $A'^3\Pi_2$ state,[57] indicating nonradiative relaxation from $B^3\Pi_{0^+}$ to $A'^3\Pi_2$ within the $B^3\Pi_{0^+}$ state radiative lifetime. The $B^3\Pi_{0^+}$, $A^3\Pi_1$, and $A'^3\Pi_2$ states are nested with small energy separations. In the charge-transfer state, similar close-lying manifolds of the $^3\Pi$ states with $\Omega = 0$, 1, and 2 are expected. Therefore, the probe transition shown in Figure 1 may not only lift wavepackets from the $B^3\Pi_{0^+}$ state but also energetically resonant ones from the $A^3\Pi_1$ and $A'^3\Pi_2$ states to the charge-transfer states.

Next, we turn to the selection of initial states. The strongest absorption of ClF corresponds to the dipole-allowed $X^1\Sigma_0^+ \rightarrow C^1\Pi_1$ transition with its Franck−Condon maximum around 280 nm. The $X^1\Sigma_0^+ \rightarrow B^3\Pi_{0^+}$ transition is mediated by spin−orbit and diabatic coupling and has its Franck−Condon maximum around 400 nm, and it is the strongest one in this spectral region. Thus, by spectral selection using the frequency-doubled wavelength of 387 nm from the Ti:Sapphire fundamental, an exclusive initial population of the $B^3\Pi_{0^+}$ state was achieved in refs 32 and 33. The resulting pump−probe spectrum serves as a reference for the wavepacket dynamics in the bound $^3\Pi$ manifold for initially exciting its $B^3\Pi_{0^+}$ state component (arrow a in Figure 1). It is reproduced in Figure 3a for parallel polarizations of the pump and probe pulses.[33] The $C^1\Pi_1$ state (arrow b in Figure 1) is selected with a pump wavelength of 280 nm from a frequency-doubled NOPA. The resulting pump−probe spectrum now reflects the dynamics of the spin-flip from $C^1\Pi_1$ to $B^3\Pi_{0^+}$ and is shown in Figure 3b once more for a parallel polarization of the pump and probe pulses.[33]

The challenge remains to choose another initial triplet state among the large manifold of repulsive states. They are not directly accessible from the ground state by use of our tunable pulse sources since the transition energy is too far in the VUV. It is possible, however, to make use of the long lifetime of the $A'^3\Pi_2$ state. The repetition rate of 1 kHz of the laser leads to a spacing in time of 1 ms for subsequent excitation pulses. The pulse separation is, by more than a factor of 100, shorter than the decay time of 141 ms. In this way, a steady-state population in the $A'^3\Pi_2$ state is generated, which is vibrationally relaxed and isotropic according to the fast statistical reorientation of the internuclear axis after excitation to the $C^1\Pi_1$ state (downward arrow in Figure 1).[24] Delayed excitation of this transient

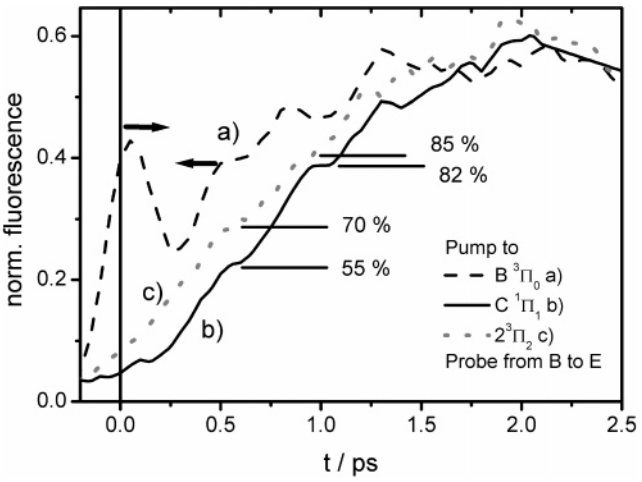

Figure 3. Fluorescence intensity of ClF from the $D'^3\Pi_2$ state by probing the $B^3\Pi_{0^+}$ population with 318 nm after a time delay t; (a) pumping the $B^3\Pi_{0^+}$ state directly with 387 nm, (b) recording spin-flip by pumping the $C^1\Pi_1$ state with 280 nm, and (c) recording $2^3\Pi_2$ relaxation by pumping the $A'^3\Pi_2$ population (from 280 nm) with an additional pulse (774 nm) to the $2^3\Pi_2$ state.

population with the Ti:Sapphire fundamental wavelength of 774 nm now allows one to pick out a new repulsive state in the Franck−Condon window for excitation from the vibrational ground state of the $A'^3\Pi_2$ state to the higher-lying repulsive states (arrow c in Figure 1). Since we start from a triplet state, another triplet state will be selected. From energy resonance and selection rule considerations, a preferential population of the $2^3\Pi_2$ state is expected, as indicated in Figure 1. In this new scheme, we have to carry out a 3 pulse experiment. With 318 nm, the $C^1\Pi_1$ state is excited to generate the $A'^3\Pi_2$ steady-state population (arrow b in Figure 1). The population in $A'^3\Pi_2$ can be increased alternatively by using a 308 nm XeCl laser at 100 Hz. In addition, a pulse with 774 nm is used to pump the $2^3\Pi_2$ state (arrow denoted c in Figure 1). A 318 nm pulse (dotted arrow $h\nu_{pr}$ in Figure 1) is variably delayed with respect to the 774 nm pulse in order to probe the $B^3\Pi_{0^+}$ dynamics after nonradiative transition to this state. The resulting pump−probe spectrum is displayed in Figure 3c.

III. Results and Discussion

III.A. Results of the Semiclassical Surface-Hopping Simulations. *III.A.1. The Ultrafast Spin-Flip in F_2@Ar.* The results of the semiclassical surface-hopping simulations for the electronic population dynamics of F_2 in Ar versus time measured from the instant of the Franck−Condon (FC) excitation of F_2@Ar into the $^1\Pi_u$ electronic state are illustrated in Figures 4 and 5. A result of central importance for our purpose is the very rapid, subpicosecond buildup of population in the $^3\Pi$ manifold of states. Figures 4 and 5 show the population of the $^3\Pi$ states, including both g and u symmetries. We note an extremely rapid buildup over a time scale of 30 fs or so. The population first peaks at $\sim$ 50 fs and then drops by about a 1/3 for t between 70 and 100 fs before rising again to a higher peak at $t \approx 180$ fs, after which a slow decline is observed. A very similar fast buildup of the $^3\Pi$ population was first observed in semiclassical F_2@Ar_{54} simulations.[31] Over the time scale shown, the difference between the results of the "cluster" and the present "periodic solid" model is modest and certainly does not change the qualitative effect. The "ultrafast spin-flip" was observed experimentally for ClF@Ar.[32] In the experiment as well, a rapid buildup of the $^3\Pi$ population in much less than a picosecond

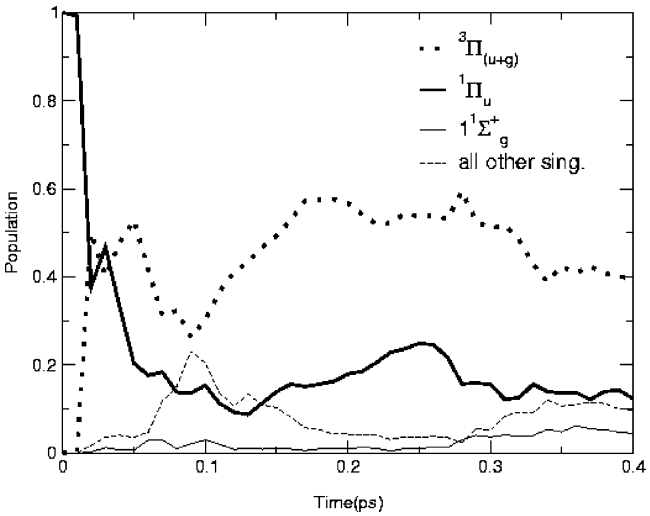

Figure 4. Caged trajectory of F_2@Ar_{255} (at 8 K); the populations of the singlet states and of the $^3\Pi$ states following Franck−Condon excitation of F_2 in solid argon into the $^1\Pi_{1u}$ state.

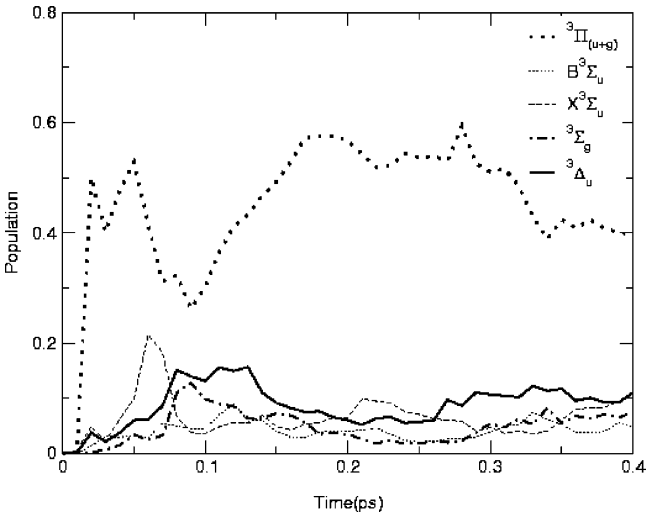

Figure 5. Caged trajectory of F_2@Ar_{255} (at 8 K); the populations of different triplet states following Franck−Condon excitation of F_2 in solid argon into the $^1\Pi_{1u}$ state.

was seen (See Figure 3). However, the analogy between the two systems cannot be viewed as quantitative. The potential surfaces of F_2 and ClF in the matrix are different; their preferred orientations in the matrix site differ, and both of these substantially affect the time scales of the atomic motions during the process. To this, one should add the fact that the experimental initial preparation (pulsed excitation, as described in section II.C) differs for the semiclassical simulation (instantaneous FC excitation of $^1\Pi_u$). Examination of the semiclassical dynamics provides the following interpretation for the ultrafast buildup of the triplet population. Upon promotion to the repulsive $^1\Pi_u$, the F−F bond distance rapidly increases. When the F−F distance reaches about 5.4 bohr or more (about twice the equilibrium distance of the molecule in the ground state), the separations between the adiabatic states become small, and the nonadiabatic interactions induce transitions between the state corresponding to $^1\Pi_u$ and adiabatic states corresponding to $^3\Pi$ with high probability. In the pure spin representation (see section II.B), the gap between $^1\Pi_u$ and $^3\Pi$ becomes small enough for transitions induced by spin−orbit coupling to occur. Collisions (in the sense of hard impact upon the matrix cage atoms) are not the mechanism by which the ultrafast spin-flip process occurs. In the present case, the F atom interactions with the matrix play a role in determining the regions where the potential surfaces intersect. However, the relevant nonadiabatic transitions precede the hard collision of the F atoms with Ar.

The ultrafast spin-flip discussed here takes place with modest spin−orbit coupling, being a consequence of the geometric location of the potential crossing. This may differ considerably from spin−orbit coupling in heavy atom[28,58] systems of very strong spin−orbit coupling. The latter case may require a different representation and coupling scheme.

After the hard collision between the F and the Ar atoms, for $t \geq 50$ fs, the strong nonadiabatic coupling transfers some population from the $^3\Pi$ state to other states, mostly to the $^3\Delta$ and $^3\Sigma$. In addition, spin−orbit coupling induces transitions also to the near-degenerate singlet states. This is the mechanism for the decrease in the population peak of $^3\Pi$ for $50 \leq t \leq 100$ fs. For $t > 100$ fs, the $^3\Pi$ population grows again, reaching a higher peak at about 180 fs. This time domain corresponds to F−F distances for which the attractive well of the $^3\Pi$ states is appreciable. This is a likely cause for the preference of this state over the others. Since the F atom loses much of its energy in the collision that occurs with the Ar, the role of the attractive well is quite significant. Extrapolating to the case of ClF, where the attractive $^3\Pi$ well is considerably deeper than that for F_2, this suggests that the propensity for the $^3\Pi$ state could be even larger in the case of ClF, at least after the first F/Ar collision, which greatly reduces the kinetic energy of the F atom. Figure 4 is restricted to $t \leq 400$ fs, that is, for the time where the 255 atom slab model with periodic boundaries is valid; see section III.A.5 below.

III.A.2. $^3\Pi$ Versus the Singlet-State Population for F_2@Ar. It is of interest to compare the population of the $^3\Pi$ states in time with that of the singlet state. Figure 4 shows the populations of the initially excited $^1\Pi_{1u}$ state, of the ground state $X^1\Sigma^+_g$, and of the sum of all other singlet states. The initially excited $^1\Pi_{1u}$ state sharply falls in population over the first 70 fs. Further falloff of the total $^1\Pi_{1u}$ population ends or becomes very weak afterward. A steady state is approximately created between nonadiabatic processes that form $^1\Pi_u$ states and those that destroy them. The sum of the other singlet states (not including the ground state) peaks at around 100 fs. The rise of this sum appears to be at the expense of the $^3\Pi$ states, following the F/Ar collision. Shortly afterward, many trajectories get trapped in these $^3\Pi$ states. In the attractive wells of the states, the amplitudes of the relative F−F motions are relatively small, and the couplings between singlet and triplet states are not large. Since the population of the dominant $^3\Pi$ becomes relatively stable, they do not feed substantial increases of the populations of the other states.

It is of interest to note that a small electronic ground-state population is formed very early on. This indicates a rather inefficient recombination, that is, for $t \leq 400$ fs, the percentage of the ground-state population is about 5%. This observation of marginal repopulation of the electronic ground state served as motivation for the neglect of nonradiative coupling between the ground and excited states in the 1D quantum model; see section II.B.

In summary, the results show that the $^3\Pi$ states are, as of $t \approx 70$ fs or even earlier, more populated than the singlet states, and except for a very brief time interval around $t \approx 100$ fs, the dominance of the $^3\Pi$ states over the singlet states is quite large. This result is useful for the construction of the reduced-dimensionality quantum model, in which unimportant states are neglected.

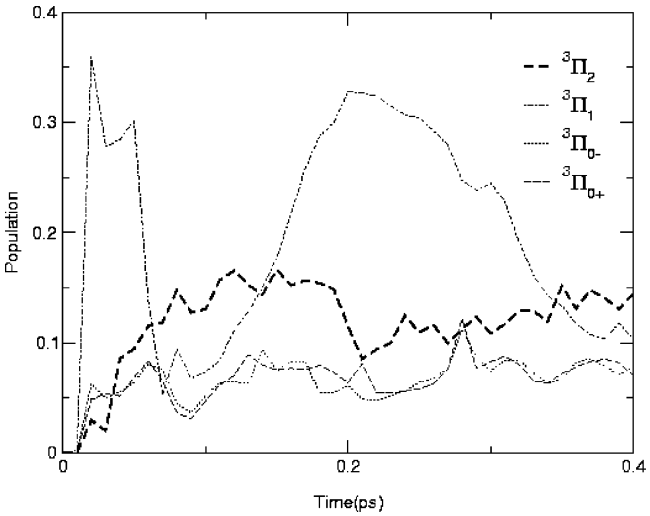

Figure 6. Caged trajectory of $F_2@Ar_{255}$ (at 8 K); the populations of different $^3\Pi_\Omega$ states of F_2 in solid argon following photoexcitation.

III.A.3. The Population of Other Triplet States: The Role of the Λ *Quantum Number for* F_2*@Ar.* The results of the previous subsection deal essentially with the role of the electronic spin in the process. To examine the role of Λ, the projection of the electronic angular momentum along the molecular axis, we compare the populations of different triplet states as a function of time in Figure 5. The message of the result is that after the $^3\Pi$ states become significantly populated, this population greatly exceeds that of the other triplets. The fluctuations of the magnitudes of these populations, for $t > 100$ fs, are not large. During most of the time interval shown, $^3\Delta_u$ has the largest population among these other triplets. However, the populations are roughly all of the same magnitude, suggesting qualitatively a statistical distribution. The characteristic that sets the $^3\Pi$ apart from the other triplets is that this state has an attractive potential well.

As emphasized previously, once a trajectory is trapped in the $^3\Pi$, especially after the F/Ar collision when the relative F−F kinetic energy is low, the F−F species is relatively stable in this state, and hops into other states, including triplets, are infrequent. We note that this approximate stability persists in our simulations for times much longer than those shown in the figures (up to $t = 1.5$ ps), as long as we address only F−F species in the cage and ignore cage exit events that, for $t >$ 600 fs, become significant.

In summary, the role of the approximate quantum number Λ in the dynamics is reflected in whether the corresponding interaction potential has an attractive well. States having an attractive well are relatively stable after the first F/Ar collision, and the F−F species can therefore be trapped with little kinetic energy and small amplitudes of relative motion, which implies less nonadiabatic coupling. There are no experimental indications of observable populations in any of the repulsive singlet or triplet states in the case of ClF. This is in qualitative accord with the results for F_2@Ar. The results support the reduced-dimensionality quantum model for ClF@Ar, in which the $^3\Sigma$ and $^3\Delta$ states are neglected.

III.A.4. The Ω *Quantum Number Role in the Photodynamics of* F_2*@Ar.* Figure 6 shows the populations in time of the states $^3\Pi_{u2}$,$^3\Pi_{u1}$,$^3\Pi_{u0^-}$, and$^3\Pi_{u0^+}$. The $^3\Pi_{u0^-}$ and the $^3\Pi_{u0^+}$ populations are equal, within the statistics of our simulations, as expected from symmetry, and the initial conditions give no preference with regard to the + or − character of the state. Following the initial buildup of the $^3\Pi$ population, the variations in the populations of the $^3\Pi_{u2}$ and $^3\Pi_{u0}$ states are moderate. However, the population of $^3\Pi_{u1}$ shows two pronounced peaks, for which this triplet dominates over the others. We do not have a simple explanation for this behavior, but some comments are suggested by the analysis. The first peak of the $^3\Pi_{u1}$ comes directly from nonadiabatic transitions of the initially excited $^1\Pi_u$ state. In the pure spin representation, $^3\Pi_{u1}$ is directly coupled by a spin−orbit interaction to the $^1\Pi_u$ state, and no additional coupling through the Ar atoms is required. Transitions from $^3\Pi_{u1}$ into $^3\Pi_{u2}$ and $^3\Pi_{u0}$ then take place, mediated by the F(^{2}P)/Ar interactions, as described in the DIM potentials. The second peak of the $^3\Pi_{u1}$ population occurs after the collision of the F atoms with the Ar "walls" as the F atom approach the mutual turning point. As noted previously, the F(^{2}P)/Ar collision leads to an increase in singlet-state populations. It seems that transitions from the singlet states go preferentially into $^3\Pi_{u1}$ more than into other triplets.

In summary the Ω state populations show dynamical preferences and are not statistically distributed.

III.A.5. Energy Transfer to the Solid for F_2*@Ar.* Figure 7 shows the kinetic energy in time for one of the F atoms (upper panel) and for an Ar atom involved in the first collision (lower panel). The results are taken from a specific trajectory but are typical also for the behavior in most other trajectories. The Ar atom that corresponds to the figure is one that lies essentially along the initial F−F axis and is therefore struck (approximately at $t \approx 35$ fs) by an F atom in a hard "collision". The kinetic energy of the above two atoms is effected, in principle, by interconversion between kinetic and potential energy, obviously a major effect, by nonadiabatic transitions that change the relevant potential surface, and by energy transfer to other atoms. The message of Figure 7 is simple: Prior to the collision between the F atom and the Ar, the lattice can be treated as static, ignoring the motions of the Ar atoms. After the F/Ar collision, the effect of the lattice atoms becomes, however, quite dramatic as the Ar atom receives a kinetic energy of >1.0 eV, this causing the onset of a shock wave that propagates further into the crystal (in the real system).

The classical calculations predict a time window over which the rigid-lattice approximation can be applied. This defines the validity range of the reduced-dimensionality quantum mechanical treatment and is therefore central to the present study. For F_2@Ar, the time window for the rigid-lattice approximation is very short (although even over this time, already some nonadiabatic transitions of importance take place and can thus be modeled by reduced-dimensionality quantum treatment). In extrapolating the result to other systems and conditions, one must keep in mind that for pulsed-laser experiments, efficient acceleration of the halogen atoms begins essentially only when the excitation pulse is fully developed. In addition, for ClF for example, the potentials are different, and the time to the F/Ar collision is different (in fact, considerably larger) as a consequence. The time window for the rigid-lattice treatment of ClF is on the order of 85 fs, as discussed previously in this paper.

Due to the periodic boundary conditions used in the semiclassical simulation for $F_2@(Ar)_{255}$, the shock wave initiated by the F/Ar collision is reflected at the ends of the simulation box and returns later to the site of the F−F, thus potentially undermining the validity of the results. This happens, however, only for $t \geq 470$ fs, outside of the time range shown in Figures 4−6.

III.A.6. Cage Exit of F Atoms in the Photodynamics of F_2*@Ar.* The results discussed in this paper are only for caged F−F species. Cage exit events were found for some of the trajectories

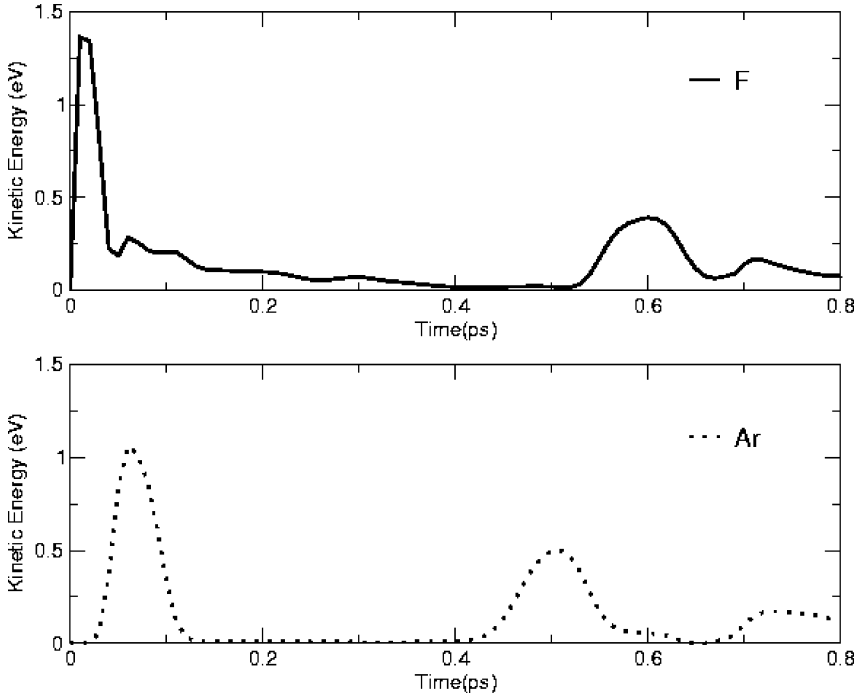

Figure 7. Caged trajectory of $F_2@Ar_{255}$ (at 8 K); kinetic energies of a F and an Ar atom following excitation of F_2 in solid Ar. Typical results from a single trajectory indicate a "collision" between the F and Ar atom at $t \approx 35$ fs.

computed, but these were not included in the analysis. Interestingly, no completely direct cage exit event was found at all in the simulations. The F atoms always recoiled into the original cage after a first collision with the argon "walls", which led to an encounter between the F atoms. Only after this encounter, as the F atoms moved again toward the argon walls, did some cage exit events take place, and their number increased with time. The earliest cage exit event in these simulations took place around $t \sim 260$ fs, toward the end of the time interval discussed here. A detailed description of cage exit in this system and the electronic state dynamics pertinent to cage exit will be published elsewhere; see also ref 50.

III.B. Results for the 1D Quantum Model of ClF@Ar. *III.B.1. Sequential Population Transfer from the Excited Singlet to the Triplet States.* The laser-driven dynamics of ClF@Ar, in particular, the resulting time evolutions of the populations $P_j(t)$ of the electronic states $j = 1-6$ corresponding to $X^1\Sigma_g^+$, $A'^3\Pi_2$, $A^3\Pi_1$, $1^3\Pi_{0^-}$, $B^3\Pi_{0^+}$, and $C^1\Pi_1$, have been evaluated using the 1D quantum model and the techniques of section II.B. We have carried out systematic investigations of the effects of the parameters for the pump laser pulse, the parameters $\gamma_{i,j}$ for the couplings between the triplet states $i,j = 2-4$, as well as g_i for the coupling between the excited singlet and triplet states; cf. eq 4. Exemplary results are shown below in Figures 8−12 for five scenarios which are related to the semiclassical and experimental results presented in sections III.A. and III.C, respectively. These examples have been chosen in order to illustrate some important general quantum properties of the electronic cage effects for this system. The corresponding laser and coupling parameters are specified in the legends for Figures 8−12.

Let us consider first the effects of a pump laser pulse, which is designed for resonant excitation of the $C^1\Pi_1$ state, with parameters similar to the experimental one; cf. section III.C. Moreover, let us choose the parameters g_j such that they correspond to coupling between the initially excited singlet state $C^1\Pi_1$ and, exclusively, one of the triplet states, specifically $A^3\Pi_1$; thus, $g_3 \neq 0$ and $g_{j\neq 3} = 0$. This choice was motivated

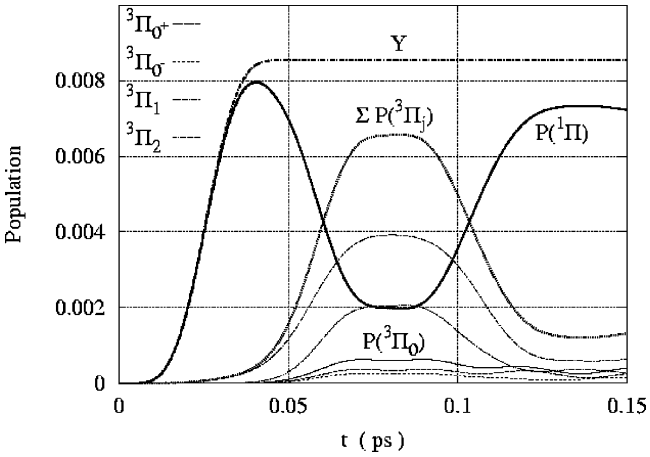

Figure 8. Quantum simulation of the electronic cage effect for the 1D model ClF@Ar driven by an UV laser pulse. The laser parameters are $\omega = 0.168\ E_h/\hbar = 36871$ c*cm^{-1} (resonant $X^1\Sigma_0^+ \rightarrow C^1\Pi_1$ transition), $E_0 = 0.0082\ E_h/ea_0$ (corresponding to $\tilde{I}_{max} = 2.35$ TW/cm^2), $t_p = 50$ fs (corresponding to $\Delta t_p = 18$ fs); cf. eqs 5−7. The molecular coupling parameters are all zero, except $g_3 = -0.00445\ E_h = 976$ hc*cm^{-1}, $\gamma_{32} = -0.006\ E_h = 1317$ hc*cm^{-1}, and $\gamma_{34} = \gamma_{35} = -0.002\ E_h = -439$ hc*cm^{-1} (corresponding to Ω-selective γ couplings; cf. eq 4). Shown are the resulting electronic populations of the initially excited $C^1\Pi_1$ state, the individual $^3\Pi$ states, the sum $^3\Pi_0$ of the two components $B^3\Pi_{0^+}$ and $1^3\Pi_{0^-}$, and the sum of all $^3\Pi_0$ states. Y is the yield of all excited states. The model is valid until approximately $t = 85$ fs.

by the corresponding exclusive spin−orbit coupling between these states for ClF in the gas phase in the present diabatic representation; see ref 52. It implies the initial preferential population transfer from the excited state $C^1\Pi_1$ to $A^3\Pi_1$. Exemplarily, let us consider the case of parameters $\gamma_{i,j}$, which correspond to couplings between the triplet state that is excited first, that is, $A^3\Pi_1$, and all other triplet states, that is, $\gamma_{3,j} \neq 0$, but without any couplings between those other states, that is, $\gamma_{i,j} = 0$ for $i,j = 2$, 4, and 5. A specific example of the parameters is given in the legend of Figure 8. This choice of

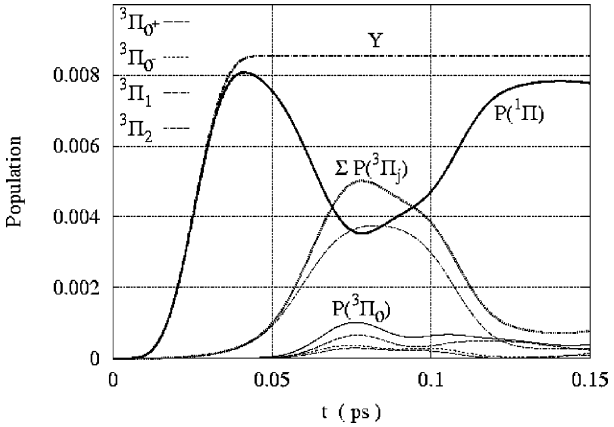

Figure 9. Same as Figure 8, except for smaller couplings $\gamma_{3,j} = -0.0015\ E_h = 329$ hc*cm^{-1}.

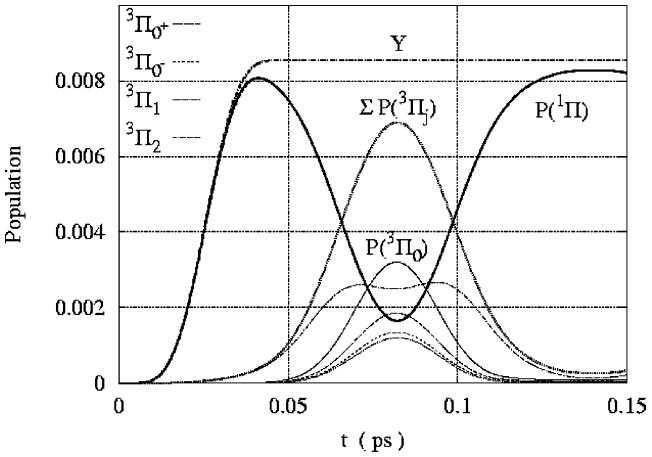

Figure 10. Same as Figure 8, except for Ω-close γ couplings $\gamma_{i,j} = -0.0015\ E_h = 329$ hc*cm^{-1}, $2 \le i \ne j \le 5$.

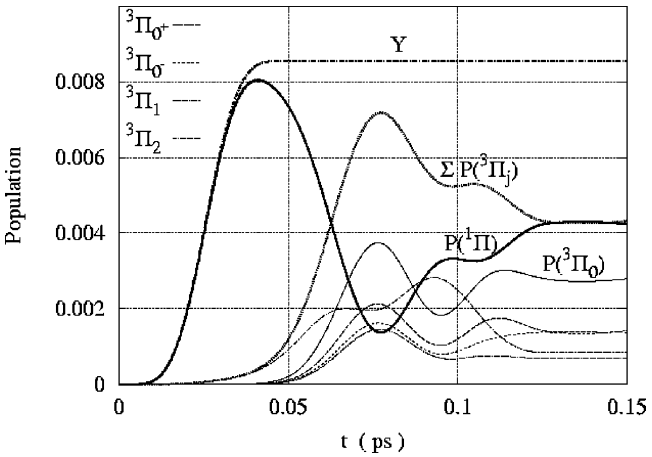

Figure 11. Same as Figure 10, except for slightly larger absolute value of $\gamma_{i,j} = -0.0020\ E_h = 439$ hc*cm^{-1}.

rather strong coupling $\gamma_{3,2}$ between the $A^3\Pi_1$ and $A'^3\Pi_2$ states as well as the smaller couplings, $\gamma_{3,4} = \gamma_{3,5}$, between $A^3\Pi_1$ and the states $B^3\Pi_{0^+}$ or $1^3\Pi_{0^-}$ implies the subsequent population transfer from $A^3\Pi_1$ preferably to $A'^3\Pi_2$ and, simultaneously yet less efficiently, to $B^3\Pi_{0^+}$ as well as $1^3\Pi_{0^-}$. The scenario of exclusive couplings $\gamma_{3,j}$ between the excited triplet state $A^3\Pi_1$ ($i = 3$) with quantum number $\Omega = 1$ and all other excited triplet states ($j = 2$, 4, and 5) with different quantum numbers Ω but without any other couplings between those states, $j = 2$, 4, and 5, will be called the case of Ω-selective γ coupling. The anticipated electronic cage effect, that is, sequential population

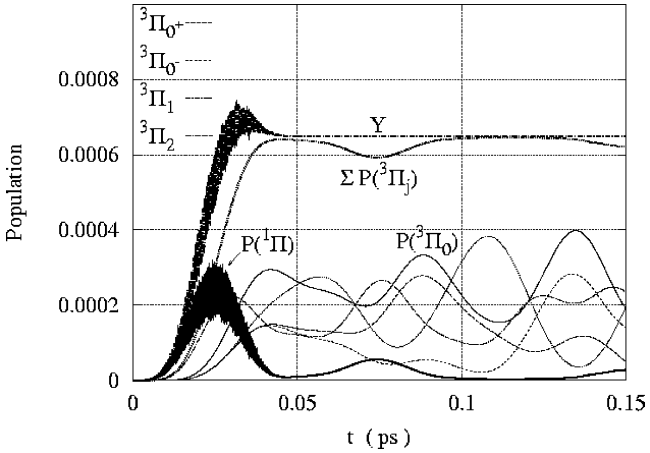

Figure 12. Same as Figure 9, except for the different laser parameters $\omega = 0.13\ E_h/\hbar = 28532$ c*cm^{-1} (corresponding to resonant $X^1\Sigma_0^+ \rightarrow A^3\Pi_1$ excitation) and $E_0 = 0.02\ E_h/ea_0$ (corresponding to $\tilde{I}_{max} = 14$ TW/ cm^2).

transfers $X^1\Sigma_0^+ \rightarrow C^1\Pi_1 \rightarrow A^3\Pi_1 \rightarrow (A'^3\Pi_2 > B^3\Pi_{0^+}, 1^3\Pi_{0^-})$, is confirmed by the resulting population dynamics, which is documented in Figure 8. Initially, that is, during a period of ≈30 fs after the time (≈40 fs, $t_p = 50$ fs) needed for laser excitation of the $C^1\Pi_1$ state, these results resemble the corresponding semiclassical results for F_2@Ar shown in Figure 6. Gratifyingly, the subsequent behaviors of the $A'^3\Pi_2$, $B^3\Pi_{0^+}$, and $1^3\Pi_{0^-}$ states are also similar for ClF@Ar and for F_2@Ar during the time of the validity (≈85 fs) of the 1D quantum model. The semiclassical result of selective population transfer between the $A^3\Pi_1$ state and other singlet states of F_2@Ar cannot be reproduced by the quantum model for ClF@Ar, however, because it does not account for those complementary singlet states.

Figure 8 also demonstrates the population dynamics of the 1D quantum model of ClF@Ar during the time from 85 to 150 fs, that is, beyond the validity (85 fs) of the 1D model. The semisinusoidal behaviors of the populations of the electronic states correspond to the vibrations of the laser-induced wavepackets in the potential wells shown in Figure 2, see ref 50, and this allows one to discover the origin of the most important observed electronic cage effects. The wavepackets run from the FC domain of the laser transition toward larger values of the ClF bond, describing initial photodissociation. At $t \approx 75$ fs, they reach the outer turning point corresponding to maximum stretch of the ClF molecule for the given preorientation along <111>. Here, all potential curves are near-degenerate, with energy gaps smaller than the corresponding couplings; cf. Figure 2. As a consequence, the couplings induce efficient population transfer, as documented in Figure 8. Subsequently, in the 1D model, the wavepackets swing back toward the original FC domain. As a consequence, most of the populations of the triplet states are transferred back to the excited singlet state, analogous to the effects which have been rationalized in ref 36. Complete back transfer is prohibited, however, by interference effects of the coherent wavepacket dynamics in the near-degenerate triplet states $j = 2-5$. These coherences cause small but nevertheless significant "quantum beats" in the population dynamics, which are obvious most easily for the states which carry rather small populations; cf. Figure 8.

Figure 9 shows the population dynamics for another example of Ω-selective γ coupling, that is, assuming equal values of $\gamma_{3,j} = -0.0015\ E_h$. Comparison with Figure 8 allows one to discover three additional effects. First, smaller sums of absolute values of the $\gamma_{3,j}$ reduce the efficiency of population transfer

from the excited triplet state $A^3\Pi_1$ to the set of the other triplet states; this is in accord with intuition. Second, equal couplings $\gamma_{3,2} = \gamma_{3,4} = \gamma_{3,5}$ do not automatically imply equal amounts of population transfer from $A^3\Pi_1$ ($i = 3$) to the other triplet states ($j = 2,4$, and 5). Instead, it turns out that population transfer to $B^3\Pi_{0^+}$ is preferred, in comparison with the transfers to $1^3\Pi_{0^-}$ and $A'^3\Pi_2$. This effect is surprising in view of the results shown in Figure 8, which might suggest a golden-rule-type behavior, that is, population transfers to states j are approximately proportional to the squares of the coupling parameters $\gamma_{3,j}$. A qualitative explanation of the apparent nonlinear behavior, that is, preferential population transfer from state $i = 3$ to $j = 2$ (instead of $j = 4$ or 5), is provided by the inset of Figure 2. Accordingly, in the domain ($R \gtrsim 5a_0$) of the most efficient (yet rather small) population transfers, all of the potential energy surfaces are near-degenerate, but $\tilde{V}_3(R)$ and $\tilde{V}_2(R)$ are closer to each other than $\tilde{V}_3(R)$ and $\tilde{V}_4(R)$ or $\tilde{V}_5(R)$, thus supporting more efficient population transfers $i = 3 \rightarrow j = 2$ compared to $3 \rightarrow 4$ or $3 \rightarrow 5$, respectively. Third, despite the fact that equal $\gamma_{3,j}$ do not yield equal amounts of population transfers, nevertheless, the resulting populations P_2, P_4, and P_5 have the same order of magnitude. As a consequence, the interference effects between states $j = 2$, 4, and 5 are more pronounced than those in the case of Figure 8 where P_2 is much larger than $P_4 \approx P_5$ due to the choice of the parameters $\gamma_{3,2} \approx 2 \cdot \gamma_{3,4} = 2 \cdot \gamma_{3,5}$. Indeed, the interference effects shown in Figure 9 are so large that they destroy the semisymmetric, near-sinusoidal behavior of the dominant population $P_3(t)$ of $A^3\Pi_1$.

III.B.2. Interferences Induced by Close Couplings between the Excited Coherent Triplet States. In order to investigate further the quantum beat phenomenon of the electronic cage effect, which has been discovered for the scenarios of Figures 8 and 9, we have carried out systematic evaluations of the electronic population dynamics, which are obtained for the same parameters, except for different couplings $\gamma_{i,j}$ of the excited triplet states. As an example, Figures 10 and 11 show the results for equal couplings between all excited triplet states $\gamma_{i,j} = -0.0015\ E_h$ and $-0.002\ E_h$, respectively. These cases of equal couplings between all triplet states $j = 2$, 3, 4, and 5 with different quantum numbers Ω will be called Ω-close γ coupling. Comparison with Figures 8 and 9 reveals the same type of initial sequential electronic population transfers $X^1\Sigma_{0^+} \rightarrow C^1\Pi_1 \rightarrow A^3\Pi_1$, which are mediated by the state-selective laser dipole ($-\mu_{1,6} \cdot E(t)$) and spin−orbit (g_3) couplings. However, the subsequent population transfers from the excited $A^3\Pi_1$ state to the other triplet states is rather different for the scenarios of Ω-selective (Figures 8 and 9) versus Ω-close γ couplings (Figures 10 and 11). Apparently, Ω-close γ couplings support stronger interferences between all of the coherent excited triplet states, resulting in much more pronounced quantum beats compared to the case of Ω-selective γ couplings. More specifically, for $\gamma_{i,j} = -0.0015\ E_h$, the quantum beats appear between the triplet state with quantum number $\Omega = 1$, which was populated first, versus the set of other triplet states with different quantum numbers $\Omega \neq 1$; cf. Figure 10. Indeed, these interferences may appear so strong that occasionally (e.g., close to 80 fs in Figure 10) the population of the first excited triplet state $A^3\Pi_1$ may even drop below the sum of the populations of the $^3\Pi_0$ states. Consequently, the time evolution of the $A^3\Pi_1$ state population may exhibit two maxima (e.g., close to 70 and 90 fs in Figure 10). Upon a first glance, this double-peak behavior of the $A^3\Pi_1$ population appears somewhat similar to the two maxima which have been discovered for the population dynamics of the $A^3\Pi_1$ for the case of F_2@Ar; cf. Figure 6. Note, however, that the origins of these similar double-peak population dynamics are entirely different. For the semiclassical simulation of F_2@Ar in full dimensionality, it is mainly due to selective population exchange between $A^3\Pi_1$ and various excited Σ states. In contrast, for the present 1D quantum model simulation, it is due to coherence effects of Ω-close coupled triplet states.

Comparison of Figures 10 and 11 shows that in the case of Ω-close γ couplings, the interference effects increase with the absolute value of the $\gamma_{i,j}$. As a consequence, the approximate symmetry of the sinusoidal-type population $P_6(t)$ of the excited singlet state and the bell-shaped $P_2(t)$, $P_4(t)$, and $P_5(t)$ or the double-peaked $P_3(t)$ for the triplet states, which are obtained for $\gamma_{i,j} = -0.0015\ E_h$ (Figure 10) is destroyed in the case of $\gamma_{i,j} = -0.002\ E_h$ (Figure 11), causing efficient singlet-to-triplet population transfers at later times (beyond the validity of the present 1D model).

Another phenomenon related to the strong quantum beat behavior of the excited triplet states for the case of Ω-close γ couplings is the extreme sensitivity of the dominance of one or the other of the triplet states, within the set of triplet states ($j = 2$, 4, and 5) which are populated after the one which is excited first ($j = 3$). For example, for the case of Figure 11, state $B^3\Pi_{0^+}$ is more excited than $1^3\Pi_{0^-}$ and $A'^3\Pi_2$, whereas other cases of Ω-close γ couplings with different parameters $\gamma_{i,j}$ may yield the reversed order. The results are even phase-sensitive, for example, they depend on the sign of the coupling parameters. Apparently, this is again due to the near degeneracy of the potential energy surfaces for the coupled triplet states, with energy gaps below the absolute values of the coupling strengths in wide domains of the molecular stretch coordinate.

III.B.3. Sequential Population Transfer from the Excited $A^3\Pi_1$ State to Other Triplet and Singlet States. Figure 12 shows the results for the same laser and coupling parameters as those in Figure 9, except for the excitation frequency, which has been tuned to excitations of the triplet states, $\hbar\omega = 0.13\ E_h$ (28532 c*cm^{-1}). We observe the apparent sequential mechanism $X^1\Sigma_0^+ \rightarrow C^1\Pi_1 \rightarrow A^3\Pi_1$ of the initial buildup of the population in the $A^3\Pi_1$ target state, mediated by transition dipole and spin−orbit couplings of the $X^1\Sigma_0^+$ and $C^1\Pi_1$ states as well as the $C^1\Pi_1$ and $A^3\Pi_1$ states, respectively. The subsequent redistribution of the population from $A^3\Pi_1$ to other triplets is rather complex, however, as it is obviously dominated by strong interference effects. Note that these interferences between all coupled triplet states exist in the entire domain of the near degeneracy of the potential energy surfaces $V_j(R)$, $j = 2-5$, that is, from the FC domain all the way to the outer turning point. Specifically, the population of the first excited triplet state $A^3\Pi_1$ dominates just for a very short initial period (≈30 fs), followed by short periods of preferential populations of the sum of the $^3\Pi_0$ states and then of the $A'^3\Pi_2$ state. Subsequently, we observe efficient population transfers between all triplet states. The apparent efficient exchange of populations between the triplet states with different quantum numbers Ω, for example, from $\Omega = 2$ to $\Omega = 0^+$, is a strong motivation to discover population transfers between triplet states also experimentally; cf. section III.C. We must emphasize, however, that any apparent selectivities of population transfers between the triplet states are again quite sensitive to the magnitudes and even to the sign of the coupling parameters $\gamma_{i,j}$. The reason for this sensitivity is similar to the corresponding sensitivity of the propensity of the dominant triplet state after laser excitation to the singlet state, cf. Figure 9, that is, interference effects of coherent wavepacket dynamics of the closely coupled triplet states $j = 2-5$.

III.C. Experimental Results and Discussion for ClF@Ar. The pump−probe spectrum of Figure 3a corresponds to a direct excitation of the $B^3\Pi_{0+}$ target state of ClF@Ar, and it serves as a reference of the detection sensitivity. The arrows indicate the passage times and directions of the wavepacket in the probe window (Figure 1), derived empirically in ref 33 from plausibility arguments and the observed structures. The molecular dynamics simulations in the $B^3\Pi_0$ state of ClF in an Ar matrix, neglecting nonradiative electronic transitions,[49] are consistent with this interpretation and thus confirm the approximate position of the probe window internuclear distance. On the basis of the simulation in ref 49, the structures in Figure 3a can be explained in the following way. The wavepacket is excited in the $B^3\Pi_{0^+}$ state above the gas-phase dissociation limit and passes, in the first 100 fs, the probe window leading to the strong first maximum, designated by the rightward arrow. The ClF molecule is oriented predominantly along <100> toward the center of a fourfold window in the Ar cage (Figure 1 in ref 49). The wavepacket has sufficient kinetic energy to cross the window, and it pushes the cage atoms outward. The wavepacket is reflected in a head-on collision from an Ar atom behind the window, crosses the cage window once more on its way back, and is detected after about 500 fs in the probe window (leftward arrow). The expected strong maximum is suppressed by wavepacket dispersion and also by the induced expansion of the cage window, which reduces the solvation energy of the ClF charge-transfer state and thus decreases the detection efficiency for the probe wavelength of 318 nm by shifting the probe window out of the wavepacket. A shorter probe wavelength weakens the influence of the solvation energy, and indeed for a probe wavelength of 302 nm (not shown), the minimum in Figure 3a around 300 fs is flattened out.[33] The collision with the cage is connected with a large energy loss, and the following wavepacket oscillations take place within the cage. The wavepacket is recorded close to the turning point leading to the subsequent maxima. A slight increase in intensity is observed up to 2 ps and attributed to vibrational energy relaxation in the ClF intramolecular potential. In this way, the kinetic energy during passage of the probe window decreases, and the detection sensitivity increases.[33] Finally, the wavepacket central energy falls below the probe window energy, leading to the decrease in intensity later on.

Here, the emphasis is on the nonradiative transition from the $C^1\Pi_1$ and $2^3\Pi_2$ states toward the target state, and this short summary of the $B^3\Pi_0$ dynamics is only required to relate the nonradiative transitions to the internal clock of the oscillating wavepacket in the cage potential. Excitation of the $C^1\Pi_1$ and the $2^3\Pi_2$ states leads to a population transfer to the target state within 1.5 ps according to Figure 3b and c, respectively. The curves a−c are normalized to equal intensity for 2 ps, and later on, all three curves show an identical decay within the noise limit. This behavior indicates that a complete population transfer takes place only in the rising part. The decay behavior beyond 2 ps is due to vibrational relaxation in the target state. The rising parts are rather similar in Figure 3b and c, and even the same (soft) steps appear in both spectra. The only apparent difference is a systematically faster rise for excitation of the $2^3\Pi_2$ state.

This general observation is already a major result when compared to the theoretical simulations. It confirms the very fast and efficient nonradiative transitions from singlet to triplet states and also among the family of triplet states.

In a more detailed interpretation, we can relate the soft steps with the wavepacket round trip history. The first passage through the window (rightward arrow) with the strong maximum for $B^3\Pi_{0^+}$ excitation leads only to a weak rise for $C^1\Pi_1$ and $2^3\Pi_2$ excitation, which is on the order of 10%. This difference indicates that the probe window is indeed most sensitive for population in the target state and that only a weak population transfer occurs from the inner turning point up to the probe window position. After the interaction with the cage and on the passage of the window on the way back (leftward arrow), a steep rise in the target state population up to 55 and 70% for the $C^1\Pi_1$ and $2^3\Pi_2$ states, respectively (compared to the $B^3\Pi_{0^+}$ excitation), is observed. This delayed rise displays, indeed, the wavepacket dynamics and goes beyond a constant rate description. Obviously, the combined effect of improving energy resonance among the states and increasing energy loss in the cage interaction funnel the wavepacket toward the target state at a large internuclear separation. The following rather flat region correlates with the well-separated states and the weak cage interaction during the inner turn. However, a second steep increase to 82 and 85% for $C^1\Pi_1$ and $2^3\Pi_2$ state excitation is detected when the wavepacket returns from a second collision with the cage. The population transfer is completed within the sensitivity of the experiment after the third cage interaction.

Turning back to the comparison with the F_2 simulation, in the more detailed inspection, we once more find a qualitative agreement in the sense that the transitions are governed by the condition of energy resonance combined with cage interaction. We relate the transition to the internal wavepacket clock because, here, a difference in time scales occurs for the ClF experiment and F_2 or ClF simulations. The F_2 and ClF simulated dynamics is faster due to scattering restricted within the first shell of the cage atoms. In addition, the assumed <111> preorientation of the ClF in the simulations leads to shorter time scales of travel to the wall. Therefore, a comparison with oscillation cycles seems to be appropriate. The simulations also contain oscillatory components in the population transfer. They do not yet show up in the experiment, which displays a stepwise rise, and it is interesting to question from where this difference originates. Note that the experiment probes the target states at the probe window only, while the computational results are for the entire configuration space. Another aspect is transfer during the first elongation. The experiment shows some transfer up to the first probe window passage but less than that predicted in the F_2 simulation. It is still open if the discrepancy displays a specific property of the two systems in the ClF and F_2 comparison or if a more distant probe window in the experiment would be the appropriate choice for ClF.

IV. Concluding Remarks

In this work, the photodynamics of dihalogens in solid argon was explored from the perspectives of three different approaches, ultrafast pulsed-laser experiments for ClF in Ar, semiclassical nonadiabatic simulations for F_2 in Ar, and reduced-dimensionality quantum treatments of ClF in Ar. The different approaches support each other on some of the aspects and, in several other respects, provide complementary information. For example, the semiclassical simulations yield a time window during which quantum reduced-dimensionality calculations are justified. This pertains both to the rigid-lattice approximation and to a limited set of electronic states, to which the treatment can be restricted. In the range of their validity, the quantum simulations make possible the description of quantum coherence effects.

The experimental and the theoretical results, though not all for the same system, converge on several important conclusions regarding the dynamics of the electronic states involved. Thus, fast population, within much less than 0.5 ps, of the $^3\Pi$ states

is found in all cases. Furthermore, in all cases, it is the $^3\Pi$ population that is found to exceed considerably, as of the early stages in the process, that of any other triplet or singlet state. This combined conclusion strengthens the interpretation given for the physical mechanism of the effect and suggests exploration of other systems where similar behavior can be found, ultrafast spin-flip in the subpicosecond range and buildup of dominant triplet populations.

There is, at least, partial evidence for other interesting nonstatistical propensities of the electronic state dynamics and for the importance of electronic angular momentum Λ and even the Ω quantum number. The results suggest that coherent control of the electronic state populations should be feasible and could lead to a more complete understanding of electronic state dynamics in the photochemistry.

Finally, from a broad perspective, the results indicate the usefulness of photochemistry in matrices as a framework for exploring quantum effects in condensed-phase chemical dynamics. Two types of quantum effects, namely, nonadiabatic transitions and interference effects reflected in coherence, were found to play a major role for the systems explored. It should be illuminating to investigate these effects by means of explicit quantum simulations of electronic coherences coupled either to classical[59−62] or even to quantum[63−66] molecular dynamics. In addition, it is a challenge to study coherence effects in sequel processes, for example, energy transfer or shock waves, beyond previous incoherent approaches.[67] Quantum and semiclassical treatments are essential for the interpretation of pronounced experimental features for these systems. It seems that this area holds considerable future promise for the continuing integration of quantum effects in condensed-phase chemical dynamics.

Acknowledgment. We would like to thank Dr. Oliver Kühn and Dr. Toni Kiljunen for the many helpful discussions and suggestions. We thank also Alexander Borowski and Heide Ibrahim for fruitful and very pleasant cooperation. The research was supported by the Deutsche Forschungsgemeinschaft in the framework of the SFB 450 project, "Analysis and control of ultrafast photoinduced reactions".

References and Notes

(1) Apkarian, V. A.; Schwentner, N. *Chem. Rev.* **1999**, *99*, 1481.
(2) Helbing, J.; Chergui, M.; Alberti, S. F.; Echave, J.; Halberstadt, N.; Beswick, J. A. *Phys. Chem. Chem. Phys.* **2000**, *2*, 4131.
(3) Alimi, R.; Gerber, R. B.; Apkarian, V. A. *J. Chem. Phys.* **1988**, *89*, 174.
(4) Alimi, R.; Gerber, R. B.; Apkarian, V. A. *J. Chem. Phys.* **1990**, *92*, 3551.
(5) Alimi, R.; Gerber, R. B. *Phys. Rev. Lett.* **1990**, *64*, 1453.
(6) Alimi, R.; Gerber, R. B.; Apkarian, V. A. *Phys. Rev. Lett.* **1991**, *66*, 1295.
(7) Alimi, R.; Gerber, R. B.; McCaffrey, J. G.; Kunz, H.; Schwentner, N. *Phys. Rev. Lett.* **1992**, *69*, 856.
(8) Slavicek, P.; Zdanska, P.; Jungwirth, P.; Baumfalk, R.; Buck, U. *J. Phys. Chem. A* **2000**, *104*, 7793.
(9) Nahler, N. H.; Baumfalk, R.; Buck, U.; Vach, H.; Slavicek, P.; Jungwirth, P. *Phys. Chem. Chem. Phys.* **2003**, 5, 3394.
(10) Kiljunen, T.; Bargheer, M.; Gühr, M.; Schwentner, N. *Phys. Chem. Chem. Phys.* **2004**, *6*, 2185.
(11) Gersonde, I. H.; Gabriel, H. *J. Chem. Phys.* **1993**, *98*, 2094.
(12) Batista, V. S.; Coker, D. F. *J. Chem. Phys.* **1996**, *105*, 4033.
(13) Batista, V. S.; Coker, D. F. *J. Chem. Phys.* **1997**, *106*, 6923.
(14) Krylov, A. I.; Gerber, R. B. *J. Chem. Phys.* **1997**, *106*, 6574.
(15) Alberti, S. F.; Halberstadt, N.; Beswick, J. A.; Echave, J. *J. Chem. Phys.* **1998**, *109*, 2844.
(16) Parson, R.; Faeder, J. *Science* **1997**, *276*, 1660.
(17) Sanford, T.; Han, S. Y.; Thompson, M. A.; Parson, P.; Lineberger, W. C. *J. Chem. Phys.* **2005**, 122, 54307.
(18) Niv, M. Y.; Krylov, A. I.; Gerber, R. B. *Faraday Discuss. Chem. Soc.* **1997**, *108*, 243.
(19) Niv, M. Y.; Krylov, A. I.; Gerber, R. B.; Buck, U. *J. Chem. Phys.* **1999**, *110*, 11047.
(20) Baumfalk, R.; Nahler, N. H.; Buck, U.; Niv, M. Y.; Gerber, R. B. *J. Chem. Phys.* **2000**, *113*, 329.
(21) Nahler, N. H.; Farnik, M.; Buck, U.; Vach, H.; Gerber, R. B. *J. Chem. Phys.* **2004**, *121*, 1293.
(22) Zadoyan, R.; Almy, J.; Apkarian, V. A. *Faraday Discuss. Chem. Soc.* **1997**, *108*, 255.
(23) Almy, J.; Kizer, K.; Zadoyan, R.; Apkarian, V. A. *J. Phys. Chem. A* **2000**, *104*, 3508.
(24) Bargheer, M.; Gühr, M.; Schwentner, N. *J. Chem. Phys.* **2002**, *117*, 5.
(25) Karavitis, M.; Segale, D.; Bihary, Z.; Pettersson, M.; Apkarian, V. A. *Low Temp. Phys.* **2003**, *29*, 814.
(26) Bihary, Z.; Karavitis, M.; Apkarian, V. A. *J. Chem. Phys.* **2004**, *120*, 8144.
(27) Bargheer, M.; Pietzner, J.; Dietrich, P.; Schwentner, N. *J. Chem. Phys.* **2001**, *115*, 9827.
(28) Gühr, M.; Ibrahim, H.; Schwentner, N. *Phys. Chem. Chem. Phys.* **2004**, *6*, 5353.
(29) Gühr, M.; Schwentner, N. *Phys. Chem. Chem. Phys.* **2005**, *7*, 760.
(30) Fiedler, S. L.; Vaskonen, K.; Ahokas, J.; Knuttu, H.; Eloranta, J.; Apkarian, V. A. *J. Chem. Phys.* **2002**, *117*, 8867.
(31) Niv, M. Y.; Bargheer, M.; Gerber, R. B. *J. Chem. Phys.* **2000**, *113*. 6660.
(32) Bargheer, M.; Niv, M. Y.; Gerber, R. B.; Schwentner, N. *Phys. Rev. Lett.* **2002**, *89*, 108301.
(33) Bargheer, M.; Gerber, R. B.; Korolkov, M. V.; Kühn, O.; Manz, J.; Schröder, M.; Schwentner, N. *Phys. Chem. Chem. Phys.* **2002**, *4*, 5554.
(34) Korolkov, M. V.; Manz, J. *Chem. Phys. Lett.* **2004**, *393*, 44.
(35) Korolkov, M. V.; Manz, J. *J. Chem. Phys.* **2004**, *120*, 11522.
(36) Chaban, G. M.; Gerber, R. B.; Korolkov, M. V.; Manz, J.; Niv, M. Y.; Schmidt, B. *J. Phys. Chem. A* **2001**, *105*, 2770.
(37) Ellison, F. O. *J. Am. Chem. Soc.* **1963**, *85*, 3540.
(38) Aquilanti, V.; Grossi, G. *J. Chem. Phys.* **1980**, *73*, 1165.
(39) Aquilanti, V.; Luzzatti, E.; Pirani, F.; Volpi, G. G. *J. Chem. Phys.* **1988**, *89*, 6165.
(40) Tully, J. C. *J. Chem. Phys.* **1990**, *93*, 1061.
(41) Tully, J.C. In *Modern Methods for Multidimensional Dynamics Computations in Chemistry*; Thompson, T. L., Ed.; World Scientific: Singapore, 1998; p 34.
(42) Nakamura, H. *Nonadiabatic Transitions*; World Scientific: Singapore, 2002.
(43) Thoss, M.; Miller, W. H.; Stock, G. *J. Chem. Phys.* **2000**, *112*, 10282.
(44) Batista, V. S.; Coker, D. F. *J. Chem. Phys.* **1999**, *110*, 6583.
(45) Topaler, M. S.; Allison, T. C.; Schwenke, D. W.; Truhlar, D. G. *J. Phys. Chem. A* **1998**, *102*, 1666.
(46) Jasper, A. W.; Zhu, C.; Nangia, S.; Truhlar, D. G. *Faraday Discuss. Chem. Soc.* **2004**, *127*, 1.
(47) Jasper, A. W.; Stechmann, S. N.; Truhlar, D. G. *J. Chem. Phys.* **2002**, *116*, 5424.
(48) Kühn, O., Manz, J., Miller, W. H., Eds. Towards Multidimensional Quantum Reaction Dynamics. *Chem. Phys.* **2004**, *304*, 1−236.
(49) Kiljunen, T.; Bargheer, M.; Gühr, M.; Schwentner, N. *Phys. Chem. Chem. Phys.* **2004**, *6*, 2932.
(50) Korolkov, M. V.; Manz, J. *Z. Phys. Chem.* **2003**, *217*, 115.
(51) Alekseyev, A. B.; Korolkov, M. V.; Kühn, O.; Manz, J.; Schröder M. *J. Photochem. Photobiol., A* **2006**, *180*, 262.
(52) Schröder, M. Ph.D. Thesis, Freie Universität Berlin, 2004; http://www.diss.fu-berlin.de/2004/43.
(53) Alekseyev, A. B.; Liebermann, Y.; Buenker, R. J.; Kokh, D. B. *J. Chem. Phys.* **2000**, *112*, 2274.
(54) Feit, M. D.; Fleck, J. A.; Steiger, A. *J. Comput. Phys.* **1982**, *47*, 412.
(55) Kosloff, R. *J. Phys. Chem.* **1988**, *92*, 2087.
(56) Marston, C. C.; Balint-Kurti, G. G. *J. Chem. Phys.* **1989**, *91*, 3571.
(57) Bargheer, M.; Dietrich, P.; Schwentner, N. *J. Chem. Phys.* **2001**, *115*, 149.
(58) Gonzalez, C. R.; Fernandez-Alberti, S.; Echave, J.; Chergui, M. *J. Chem. Phys.* **2002**, *116*, 3343.
(59) Yagi, K.; Takatsuka, K. *J. Chem. Phys.* **2005**, *123*, 224103.
(60) Langer, H.; Doltsinis, N. L.; Marx, D. *ChemPhysChem* **2005**, *6*, 1734.
(61) Kunert, T.; Grossmann, F.; Schmidt, R. *Phys. Rev. A* **2005**, *72*, 023422.
(62) Ushiyama, H.; Takatsuka, K. *Angew. Chem.* **2007**, *119*, 593.
(63) Kono, H.; Sato, Y.; Tanaka, N.; Kato, T.; Nakai, K.; Koseki, S.; Fujimura, Y. *Chem. Phys.* **2004**, *304*, 203.
(64) Kreibich, T.; Leeuwen, R. V.; Gross, E. K. U. *Chem. Phys.* **2004**, *304*, 183.
(65) Paramonov, G. K. *Chem. Phys. Lett.* **2005**, *411*, 350.
(66) Palacios, A.; Bachau, H.; Martin, F. *Phys. Rev. Lett.* **2006**, *96*, 143001.
(67) Blumen, A.; Lin, S. H.; Manz, J. *Chem. Phys.* **1978**, *69*, 881.